Biochemistry and Cell Biology

OPEN ACCESS | Article

The 3′ terminal region of Zika virus RNA contains a conserved G-quadruplex and is unfolded by human DDX17

Dannielle L. Gemmill[a], Corey R. Nelson[a], Maulik D. Badmalia[a], Higor S. Pereira[a], Liam Kerr[a], Michael T. Wolfinger[b,c,d], and Trushar R. Patel[a,e,f]

[a]Alberta RNA Research and Training Institute & Department of Chemistry and Biochemistry, University of Lethbridge, Lethbridge, AB T1K 3M4, Canada; [b]Bioinformatics and Computational Biology, Faculty of Computer Science, University of Vienna, Währinger Strasse 29, 1090, Vienna, Austria; [c]Department of Theoretical Chemistry, University of Vienna, Währinger Strasse 17, 1090, Vienna, Austria; [d]RNA Forecast e.U., 1140 Vienna, Austria; [e]Department of Microbiology, Immunology and Infectious Disease, Cumming School of Medicine, University of Calgary, Calgary, AB T2N 4N1, Canada; [f]Li Ka Shing Institute of Virology and Discovery Lab, University of Alberta, Edmonton, AB T6G 2E1, Canada

Corresponding author: **Trushar R. Patel** (email: trushar.patel@uleth.ca)

Abstract

Zika virus (ZIKV) infection remains a worldwide concern, and currently no effective treatments or vaccines are available. Novel therapeutics are an avenue of interest that could probe viral RNA-human protein communication to stop viral replication. One specific RNA structure, G-quadruplexes (G4s), possess various roles in viruses and all domains of life, including transcription and translation regulation and genome stability, and serves as nucleation points for RNA liquid-liquid phase separation. Previous G4 studies on ZIKV using a quadruplex forming G-rich sequences Mapper located a potential G-quadruplex sequence in the 3′ terminal region (TR) and was validated structurally using a 25-mer oligo. It is currently unknown if this structure is conserved and maintained in a large ZIKV RNA transcript and its specific roles in viral replication. Using bioinformatic analysis and biochemical assays, we demonstrate that the ZIKV 3′ TR G4 is conserved across all ZIKV isolates and maintains its structure in a 3′ TR full-length transcript. We further established the G4 formation using pyridostatin and the BG4 G4-recognizing antibody binding assays. Our study also demonstrates that the human DEAD-box helicases, $DDX3X_{132\text{-}607}$ and $DDX17_{135\text{-}555}$, bind to the 3′ TR and that $DDX17_{135\text{-}555}$ unfolds the G4 present in the 3′ TR. These findings provide a path forward in potential therapeutic targeting of DDX3X or DDX17's binding to the 3′ TR G4 region for novel treatments against ZIKV.

Key words: Zika virus, 3′ terminal region, G-quadruplex, BG4 antibody, DDX17, helicase assay

Introduction

Zika virus (ZIKV) is an endemic, neurovirulent arbovirus whose primary vectors are *Aedes aegypti* and *Aedes albopictus* mosquitoes. Its primary transmission mode is the horizontal transfer of mosquito-infectious saliva during blood feeding (Musso and Gubler 2016). Currently, the Centers for Disease Control and Prevention has designated 86 countries as ZIKV risk areas (Prevention 2022). ZIKV is popularly known for the 2015/2016 epidemic in Brazil; during that time, it was revealed that the virus can be vertically transmitted from an infected pregnant woman to their fetuses, which can lead to congenital disabilities such as microcephaly in utero (Tang 2016). ZIKV can also cause debilitating symptoms in adults, including Guillain-Barré Syndrome, fever, rash, headaches, and joint pain, and can also be sexually transmitted (Barzon et al. 2016; Mansuy et al. 2016; Tang 2016). Currently, there are no treatments or vaccines available (USA Food and Drug Administration 2022). ZIKV possesses a positive-sense, non-segmented RNA genome of ~10.4 kb, which is composed of a 5′ terminal region (TR) (~108 nt), three structural genes—capsid (C), membrane (prM), and envelope (E)—and seven nonstructural genes—NS1, NS2A, NS2B, NS3, NS4A, NS4B, and NS5, followed by a long, 3′ TR (~432 nt). The TRs play vital roles in viral genome cyclization, which regulates viral transcription and translation, and they alter host mRNA turnover, suppresses interferon response, and modulate the host-cell environment (Donald et al. 2016; Chavali et al. 2017; Sirohi and Kuhn 2017; Sanford et al. 2019; Schneider and Wolfinger 2019; Michalski et al. 2019; Wolfinger 2021).

An area of interest for antiviral targeting is G-quadruplexes (G4s)—noncanonical structures identified in all domains of life and almost all viral groups in the Baltimore classification (Ruggiero and Richter 2020). Viral G4s are known to play

Fig. 1. Schematic of a G-quadruplex and RNA transcripts under study. A schematic of a G4 in parallel conformation with monovalent cations coordinated in the core of the stacked guanines is shown in (A). Transcripts that were used in the experiments, with the potential G-quadruplex sequence at the ends of the 3′ terminal region (TR) (green) and 3′ SL (blue) are shown in (B). The G4 mutant is shown in red, along with the G4 mutation sequence shown below compared to the wild-type sequence.

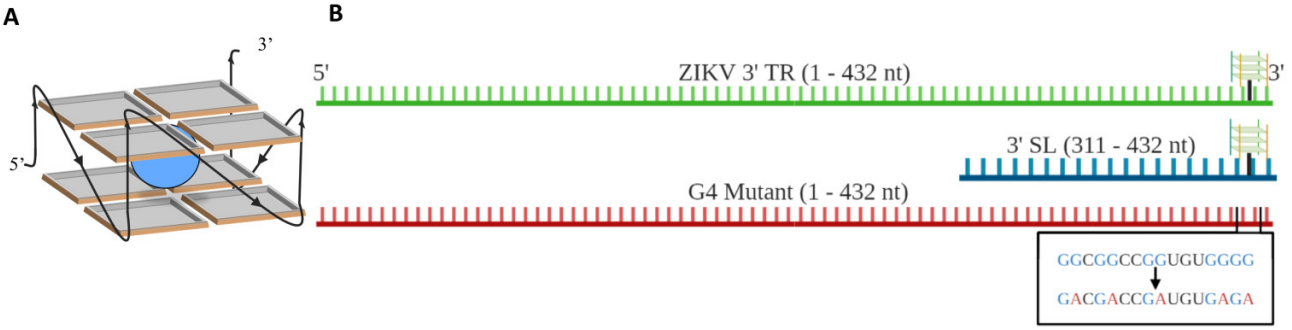

critical roles throughout regulatory processes in their life cycles, such as transcriptional and translational activities, as well as alternative splicing (Patel et al. 2000; Métifiot et al. 2014; Murat et al. 2014; Meinke et al. 2016). G4 structures consist of at least two consecutive guanine tetrads in close proximity Hoogsteen base pairing with each other in both DNA and RNA (Wang and Patel 1993; Burge et al. 2006; Bhattacharyya et al. 2016), altogether stabilized by a monovalent cation (preferably K^+) at the coordinating site (Fig. 1A). DNA G4s can adopt parallel, antiparallel, and hybrid conformations, whereas RNA G4s exclusively adopt propeller-type parallel topology due to the 2′-OH preventing syn-conformation torsion angles (Fay et al. 2017) (Fig. 1A).

It has been shown that many human proteins, including DExD-box helicases, interact with G4s (Linder et al. 1989; Brázda et al. 2014; Zhang et al. 2021). The DExD-box family proteins are involved in a wide range of functions, including embryonic development, cell proliferation, hematopoiesis, metabolism, immune response, cancer pathogenesis, inflammation, autoimmune diseases, and influence of viral replication (Meier-Stephenson et al. 2018; Andrisani et al. 2022). We have previously demonstrated that the DEAD-box helicases, $DDX3X_{132\text{-}607}$ or $DDX17_{135\text{-}555}$, interact and unfold the intergenic region (IGR) and 5′ noncoding region of the Rift Valley fever virus and the Japanese encephalitis and Zika virus 5′ TRs, respectively (Nelson et al. 2020; Nelson et al. 2021). DDX3X has been reported as a critical factor required for dengue and hepatitis C viral replication and as an inhibitory factor for West Nile virus replication (Ariumi et al. 2007; Brai et al. 2019). It has also been shown to interact with RNA G4s. Conversely, it is unclear if DDX17 directly binds to G4s, since it is involved in G4 binding with other proteins, but no direct interaction has been demonstrated (Fortuna et al. 2021; Dardenne et al. 2014). A previous study on the identification of the ZIKV genomic RNA structure of both African and Asian/American lineages using selective 2′-hydroxyl acylation analyzed by primer extension identified a conserved, canonical stem-loop structure within the 3′ TR (classified as the 3′ stem-loop [SL]) (Li et al. 2018). Interestingly, a study by Fleming et al. (2016) found potential G-quadruplex sequences within ZIKV using the quadruplex-forming G-rich sequences Mapper, and they identified and characterized a G4 contained in the 3′ SL, albeit using a 25-mer oligo short-range interaction approach (Kikin et al. 2006; Fleming et al. 2016). From the perspective of long-range RNA interactions, it is still unclear if a G4 is maintained in the 3′ SL. Additionally, a previous study indicated that conformational switching could occur between G4 and canonical RNA structures, as in the case of this study, a hairpin (Bugaut et al. 2012). These events are based on the proximity of specific mono and divalent cations, which are altogether generated by RNA liquid–liquid phase separation (X. Liu et al. 2021). From these recent discoveries, the 3′ SL could exist as canonical and noncanonical states based on ion proximity.

Because of the lack of treatment options for ZIKV, investigation of alternative targets within the viral structure or life cycle is being explored, and G4s is one of them (Majee et al. 2021). The G4 binding molecules, Braco-19, TMPyP4, Berberine, NiL, 360 A, and pyridostatin (PDS), have all been shown to interact with ZIKV G4s in vitro and cell culturing assays and showed that these molecules altogether reduce viral replication and protein production to varying degrees (Majee et al. 2021; Zou et al. 2021). It remains unclear if the 3′ TR G4 exists in a larger RNA structure containing long-range interactions, as previous studies focus on a short-range approach using short oligos. Moreover, deciphering the various human proteins that interact with this G4 could provide insight into its function during viral replication.

In this study, we investigated the presence of a G4 in the full-length ZIKV 3′ TR. For this purpose, we first used bioinformatics analyses to demonstrate that the 3′ SL G4 sequence is present in multiple ZIKV isolates. By implementing a long-range interaction approach with long RNA transcripts of the 3′ TR (432 nt) and 3′ SL (104 nt) (Fig. 1B), we were able to identify the presence of a G4 in the 3′ TR transcript using the BG4 antibody, TMPyP4, and PDS, which all specifically bind to G4s. Subsequently, we elucidated that human $DDX3X_{132\text{-}607}$ and $DDX17_{135\text{-}555}$ interact with the 3′ TR and that $DDX17_{135\text{-}555}$ unwinds the G4 present in the 3′ SL in an ATP-dependent manner.

Materials and methods

Bioinformatics analysis of conserved G4s in the 3′ TR

ZIKV viral genome data were downloaded from NCBI GenBank on 14 January 2021, comprising 1028 ZIKV isolates. Filtering for isolates that cover the complete G4-containing 3′ SL regions was performed with an Infernal covariance model (Nawrocki and Eddy 2013) constructed from the 3′ SL seed alignment of the Spondweni group featured in the viRNA GitHub repository (https://github.com/mtw/viRNA), resulting in 113 ZIKV isolates. Filtering these for a nonredundant set of 3′ SL regions resulted in a total of 14 representative ZIKV isolates. The ZIKV isolates from Haiti used in this study (KU509998.3) are identical to strain MN577544.1, featured in our nonredundant set, throughout the entire 3′ SL region. A structural multiple sequence alignment of the 3′ SL region of 14 representative ZIKV isolates was computed with LocARNA (Will et al. 2007) and visualized with Jalview (Clamp et al. 2004).

RNA transcript expression of 3′ TR, 3′ SL, and G4 mutant

The ZIKV 3′ TR (10375–10807) (432 nt) sequence was derived from the ZIKV isolate from Haiti (GenBank: KU509998.3) (Lednicky et al. 2016). This isolate also has a nearly identical sequence to the Asian/American lineage, one of the predominant lineages across the globe (Beaver et al. 2018). We designed three plasmid constructs from this sequence containing the full 3′ TR, the 3′ SL, and a 3′ TR with the G4 sequence mutated (G4 mutant). The G4 mutant construct was designed wherein five nucleotide mutations were made (5′-GGCGGCCGGUGUGGGG-3′ → 5′-GACGACCGAUGUGAGA-3′) (Fig. 1B) in the hypothesized G4 sequence to disrupt the G4 formation. All constructs were made using pUC57-Kan plasmids with a T7 promoter upstream of the desired transcript, with an *Xba*I cut site at the end of the transcript to linearize the plasmid such that T7 polymerase dissociates during in vitro transcription (IVT) reactions. The 3′ TR and 3′ SL plasmid constructs were commercially synthesized by Integrated DNA Technologies, and BioBasic synthesized the G4 mutant.

The synthesized plasmids were transformed into competent *Escherichia coli* NEB5α cells (New England Biolabs), and the cells were further propagated to replicate the plasmid DNA for IVTs. The plasmid DNA was extracted, linearized using *Xba*I restriction digestion, and subsequently used for IVT reaction. The T7 polymerase-based (expressed and purified in-house) IVT reaction was performed by mixing transcription buffer (200 mM Tris-Cl [pH 7.5], 75 mM $MgCl_2$, 10 mM spermadine, and 50 mM NaCl), 100 mM DTT, 25 mM nucleoside triphosphates, 100 mM guanosine monophosphate, 0.5 U/μL IPPase, 10 μM T7 polymerase, Ribolock, and the digested plasmid and performed for 3 h at 37 °C. This was followed immediately by purification via size-exclusion chromatography (SEC) using a Cytiva Superdex 200 Increase 10/300 GL for the ZIKV 3′ SL and a Sephacryl S-400 HR for the 3′ TR and G4 mutant RNA (Fig. S1A/B). The columns were pre-equilibrated in G4 buffer (10 mM HEPES [pH 7.5] and 100 mM KCl). For purity analysis, the peak fractions were analyzed on a 2% agarose gel (Fig. S1C). The purified RNA was then ethanol precipitated at −80 °C in preparation for RNA labeling for subsequent experiments.

Expression and purification of BG4 antibody, as well as $DDX17_{135\text{-}555}$ and $DDX3_{132\text{-}607}$ proteins

The plasmid coding for the BG4 antibody was obtained from Addgene (pSANG10-3 F-BG4) and transformed into *E. coli* BL21 DE3 for protein expression. The transformed cells were grown at 37 °C until the optical density reached 0.6 at 600 nm. Subsequently, cells were induced with 1 mM isopropylthio-β-galactoside and were grown for 16 h at 16 °C, followed by cell harvesting through centrifugation. The harvested cells were resuspended in lysis buffer (50 mM Tris-Cl [pH 7.5], 500 mM NaCl, 0.2% tween, 5% glycerol, 5 mM β-mercaptoethanol, and 10 mM imidazole), supplemented with 0.1 mg/mL lysozyme, 200 units of DNase I (Thermofisher), 2 mM PMSF, as well as protease inhibitors (pepstatin, aprotinin, and AEBSF) from Biobasic. The cell suspension was sonicated and clarified using centrifugation (30 000× *g*); the clarified lysate was loaded onto a 1 mL Histrap high-performance column from Cytiva mounted on an Äkta Start system and purified using an elution gradient from 10 to 150 mM imidazole supplemented to the lysis buffer. The fractions were purified via SEC using a Superdex 75 increase 10/300 GL (Cytiva) pre-equilibrated with 1X PBS mounted on an Äkta Pure system (Fig. S2). The fractions were analyzed on a 12% SDS-PAGE gel, pooled, and concentrated to 14 μM and stored at −20 °C until further use.

$DDX3X_{132\text{-}607}$, $DDX17_{135\text{-}555}$, and DDX17 mutants are altogether truncated versions of the protein (Fig. S3A), and each was expressed according to protocols described previously using an *E. coli* expression system similar to the BG4 antibody (Nelson et al. 2020, 2021) (Fig. S3B). DDX17 mutant was also purified using a pET28a cloned vector with glycine mutations on amino acids which coordinate ATP hydrolysis; the Q motif, which interacts with the adenine of ATP; and motifs 1 and 2 in the ATP binding domain, which interact with the triphosphate (Fig. S3A,C) (Ali 2021*a*; Ali 2021*b*; Tanner et al. 2003). The mutant assays were performed to prevent ATP hydrolysis, and consequently, helicase activity.

Alexa Fluor 488 labeling of the RNA

Each purified RNA transcript was labeled at the 5′ end with Alex fluor 488. Note that 1.25 mg of 1-ethyl-3- (3-dimethylaminopropyl) carbodiimide hydrochloride was mixed with 8 μL of concentrated RNA in water and 5 μL Alexa Fluor 488 in 0.2 M KCl, and 20 μL of 0.1 M imidazole (pH 6). All reactions were incubated at room temperature for 18 h. The RNA was then diluted in 460 μL of G4 buffer (10 mM HEPES [pH 7.5] and 100 mM KCl) and loaded onto a Cytiva Superdex 200 Increase 10/300 GL to purify the labeled RNA from the unlabeled fluorophore. Each RNA sample was then collected and heat-cooled at 95 °C for 5 min, followed by room temperature incubation for 15 min. The RNA was tested for fluorescence counts on the NanoTemper Technologies Monolith NT.115 microscale thermophoresis (MST) device to ensure optimal labeling for downstream experiments, similar to previ-

ous experiments that used Alex Fluor 488 for labeling their nucleic acids (Yoo et al. 2004; Johnson et al. 2006; Kynast et al. 2004). The labeled RNA was then vitrified in liquid nitrogen and stored at −80 °C until downstream experimentation.

Interaction studies using microscale thermophoresis

A Monolith NT.115 MST from NanoTemper Technologies was used to evaluate the affinity of RNA constructs with their ligands. The ZIKV 3′ TR, G4 mutant, and 3′ SL RNA transcripts were evaluated at 80 nM at 100% excitation at medium MST power for the BG4 binding affinity and PDS binding check runs. For the MST binding studies, the samples were serially diluted two-fold in the MST capillaries with concentrations ranging from 6.8 μM – 0.8 nM for BG4, 7 μM – 14.6 nM for $DDX3X_{132\text{-}607}$, and 19 μM – 0.58 nM for $DDX17_{135\text{-}555}$. All MST data were collected in triplicate at room temperature using the Nano-Blue filter and medium IR-laser power for BG4, while high power was used for $DDX3X_{132\text{-}607}$ or $DDX17_{135\text{-}555}$. The dissociation constants were calculated using the Monolith NT.115 analysis software by plotting the ligand % bound, and for the PDS runs, the average response amplitude was recorded in triplicate, and the Monolith NT.115 analysis software provided the signal-to-noise ratio values.

Electrophoretic mobility shift assays (EMSAs) were performed to support the MST binding data (Fig. S4) with the ZIKV 3′ TR mixed with two-fold serial diluted concentrations of $DDX3X_{132\text{-}607}$ or $DDX17_{135\text{-}555}$. Furthermore, the oligonucleotides used in the MST helicase assay were also mixed with $DDX3X_{132\text{-}607}$ or $DDX17_{135\text{-}555}$ to ensure that the helicase assay results on the MST were a result of the 3′ SL being unwound, not the oligo binding to the protein. The labeled ZIKV RNA was scanned on Cy2, whereas the oligo was scanned on Cy5.

Unwinding assays of the ZIKV 3′ TR G4

To assess the ability of $DDX3X_{132\text{-}607}$ and $DDX17_{135\text{-}555}$ to unwind the noncanonical structured area in the 3′ SL, we used MST and a complementary RNA (5′-AGUUUCCACCACGCUGGCCGCCA-3′) that would only base pair to the G4 portion of the target RNA, if it was unfolded by $DDX3X_{132\text{-}607}$ or $DDX17_{135\text{-}555}$, as performed previously (Nelson et al. 2020, 2021). When fluorescence and (or) migratory differences occur between the BSA control and the helicase, this provides evidence that the helicase unfolded the noncanonical region, as the oligo base pairing causes a change in fluorescence, shape, charge, and (or) hydration shell of the target RNA (Huang and Zhang 2021). The reaction was performed using 1 μM ZIKV 3′ SL RNA sample, 4.25 μM ATP, 40 nM Cy-5 DNA Oligo, and 20 μM of either $DDX3X_{132\text{-}607}$ or $DDX17_{135\text{-}555}$. BSA was selected as a negative control. The reaction was incubated for 15 min prior to the measurements. The experiments were performed eight times in total over two binding check runs on the Nanotemper Monolith NT.115. At 50% excitation and medium MST power, the signal-to-noise ratio was assessed for each run to determine successful unwinding activity, where, again, a signal-to-noise ratio of ≥5 indicates that binding is occurring.

A spectrofluorimetric unwinding assay was also performed using a Quanta Master 60 fluorescence spectrometer (Photon Technology International). The reactions were performed using a mixture of 2 μM protein, 50 nM RNA, and 3.5 μM ThT—a well-characterized G4 binding biosensor (Xu et al. 2016). The mixture was incubated for 5 min to allow ThT to bind to the G4 on the RNA, followed by a fluorescence measurement taken at 425 nm excitation and emission collected from 450–510 nm with a step size of 1 nm increments. Following initial data collection, 60 μM of ATP was titrated into the mixture, followed by a 5 min incubation to allow the helicase to unfold the G4, preventing ThT from binding, as the G4s is unfolded, and the same fluorescence parameters were used to collect the emission. The change in fluorescence was then plotted ($n = 3$), and a *t*-test was performed to check for statistical significance. $DDX17_{135\text{-}555}$, $DDX3X_{132\text{-}607}$, and a control, BSA, were used to validate the MST results of unwinding.

Results

The G4 sequence contained in the 3′ SL of the 3′ TR is conserved across the globe in ZIKV isolates

To obtain a comprehensive view of the sequence diversity within the 3′ TR of all known ZIKV isolates, we collected all complete ZIKV genomes from NCBI GenBank (Clark et al. 2016) and extracted the genomic regions that fold into the 3′ SL element. Filtering for nonredundant sequences in the 3′ SL region resulted in 14 representative ZIKV isolates, comprising both African and Asian/American ZIKV lineages. A structural multiple sequence alignment is shown in Fig. 2, highlighting strong primary sequence conservation of the region of interest that could potentially form a G4 structure.

ZIKV 3′ TR contains a G4 structure

We performed MST binding checks with PDS, and binding affinity studies with the BG4 antibody, altogether with the 3′ TR of ZIKV to investigate if the 3′ TR contains a G4 (Fig. 1A). PDS is a small molecule that selectively binds to the top quartet of a G4 and stabilizes the noncanonical structure (Rodriguez et al. 2012; Zhang et al. 2014; Moruno-Manchon et al. 2017; Hou et al. 2022). PDS showed a significant response amplitude in the 3′ TR and 3′ SL compared to the G4 mutant in samples treated with PDS versus no PDS (Fig. 3A). These results suggest that any potential for the G4 formation in the G4 mutant is significantly impeded or nonexistent, as PDS is below the signal-to-noise (SNR) threshold, and the response amplitude is significantly lower than the 3′ TR and 3′ SL. The Nanotemper analysis software states that a binding event evidently occurs when the SNR value is ≥5 when comparing treated versus untreated samples. Previously, it was demonstrated that a ∼20 nt oligo from the 3′ SL of ZIKV contains a G4 structure using PDS (Hou et al. 2022) indicating that PDS is a reliable molecule in the study/identification of G4s.

We further investigated the presence of a G4 using an antibody (BG4) that specifically targets the G4 structure. The BG4 antibody is a well-established, reliable antibody that has been widely used to identify G4s of both DNA and RNA in vivo and in vitro (Biffi et al. 2013, 2014*a*, 2014*b*; Byrd et al.

Fig. 2. The 3′ stem-loop (SL) G4 sequence is conserved across 1028 Zika virus (ZIKV) isolates. Fourteen nonredundant ZIKV 3′ SL sequences from African and Asian/American lineages were aligned using the LocARNA software (Will et al. 2007). The consensus sequence and its accompanying dot-bracket notation are also included, noting that the software predicts a canonical structure within the dot-bracket notation.

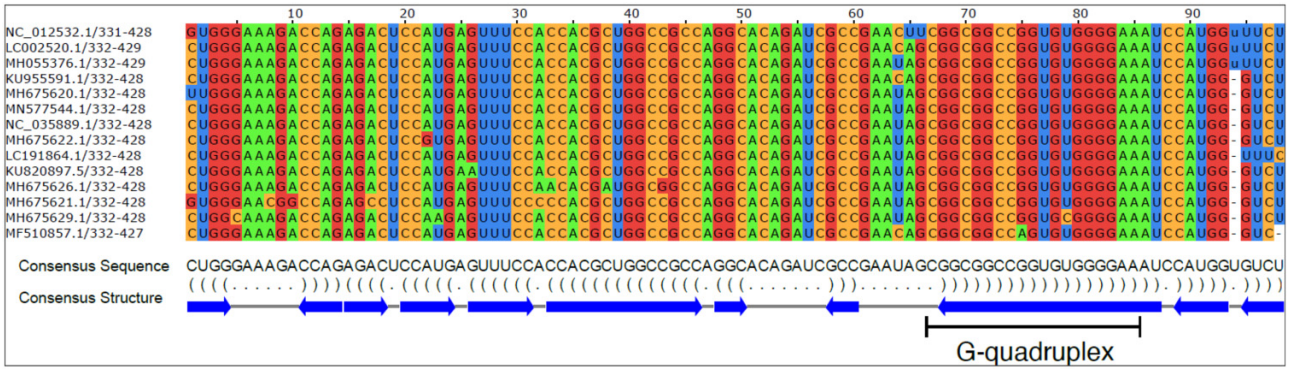

Fig. 3. A G4 exists in the 3′ stem-loop (SL) of the 3′ terminal region (TR). The change in normalized fluorescence data with RNA alone compared to RNA + pyridostatin (PDS) ($n = 3$) is shown in (A). Binding affinities of BG4 and TMPyP4 with Zika virus (ZIKV) 3′ SL (blue), 3′ TR (green), and 3′ G4 mutant (red) are shown in (B and C). The determined K_d for each transcript for BG4 were as follows: 3′ SL = 0.0106 ± 0.0023 μM, 3′ TR = 1.27 ± 0.087 μM, 3′ G4 mutant = 11.11 ± 1.71 μM, and for TMPyP4: 3′ SL = 0.0471 ± 0.0079 μM, 3′ TR = 0.0339 ± 0.0117 μM, 3′ G4 mutant = no binding ($n = 3$).

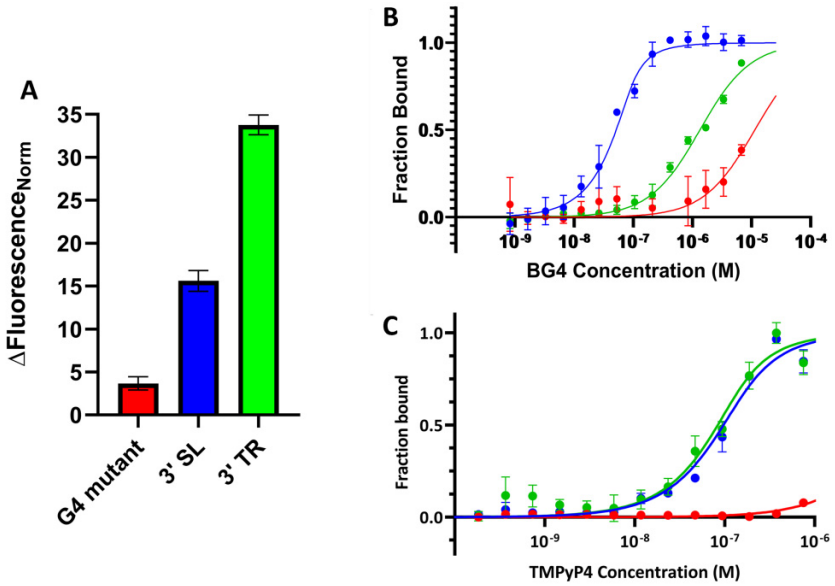

2016; Mao et al. 2018; David et al. 2019; Canesin et al. 2020; Javadekar et al. 2020; Xu et al. 2020; Komůrková et al. 2021; Varshney et al. 2021). The MST experiments using the BG4 antibody suggested that BG4 interacts with the 3′ SL at the nanomolar range, 0.0106 ± 0.0023 μM (Fig. 3B, blue line), whereas the binding affinity of the 3′ TR was determined to be 1.27 ± 0.08 μM (Fig. 3B, green line). The binding studies of BG4 with G4 mutant suggested a K_d of 11.11 ± 1.71 μM (Fig. 3B, red line), which is 10-fold weaker compared to the wild-type sequence. This change in the K_d value suggests that the mutant sequence cannot form a G4. A potential reason for the kinetic differences between the 3′ SL and 3′ TR could be due to steric/structural hindrance specific to the ZIKV 3′ TR that is not present in the 3′ SL, as previous literature shows that kinetics can differ depending on access to the binding site (Dupuis et al. 2014). These data were further supported by performing binding affinity MST studies with TMPyP4 (Fig. 3C), which is also a well-characterized G4 binding/unfolding small molecule (Morris et al. 2012; Zamiri et al. 2014; Ji et al. 2020). The affinity determined for each RNA with TMPyP4 was as follows: 3′ SL = 0.0471 ± 0.0079 μM, 3′ TR = 0.0339 ± 0.0117 μM, and 3′ G4 mutant = no binding.

DDX3X$_{132\text{-}607}$ and DDX17$_{135\text{-}555}$ interact with the ZIKV 3′ TR

The interaction studies between the ZIKV 3′ TR and the human helicases, DDX3X$_{132\text{-}607}$ and DDX17$_{135\text{-}555}$, were per-

Fig. 4. $DDX3X_{132\text{-}607}$ and $DDX17_{135\text{-}555}$ bind to the 3′ TR. Microscale thermophoresis (MST) traces demonstrate the interaction of the 3′ terminal region (TR) of Zika virus (ZIKV) with $DDX3X_{132\text{-}607}$ (green) and $DDX17_{135\text{-}555}$ (blue). RNA concentration was a constant 50 nM, while the dilution series started from 19 μM for $DDX17_{135\text{-}555}$ and 15 μM for $DDX3X_{132\text{-}607}$ ($n = 3$). Measurements were performed using 20% excitation and high MST power. The K_d was determined to be 1.16 ± 0.02 μM for $DDX17_{135\text{-}555}$ and 3.70 ± 0.10 μM for $DDX3X_{132\text{-}607}$.

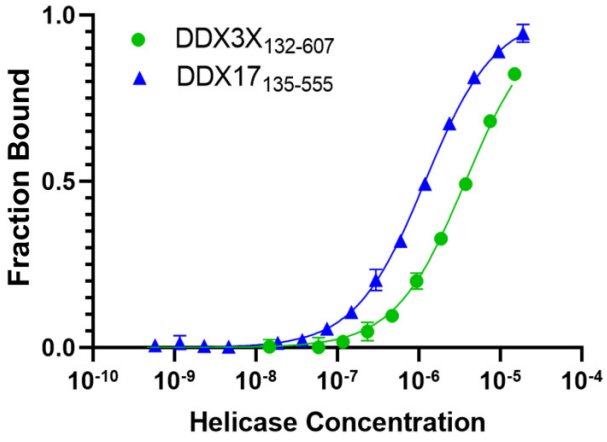

formed using MST. Figure 4 shows the binding affinities of $DDX17_{135\text{-}555}$ and $DDX3X_{132\text{-}607}$ with the ZIKV 3′ TR, with a K_d of 1.16 ± 0.02 μM and 3.70 ± 0.10 μM, respectively. Additionally, these interactions were confirmed through a native-PAGE and agarose EMSA where a shift is observed in concentrations measured around the K_d for both $DDX3X_{132\text{-}607}$ and $DDX17_{135\text{-}555}$ (Fig. S4). These affinities align with previous studies on the ZIKV 5′ TR, which suggested that $DDX3X_{132\text{-}607}$ binds with an affinity at 7.05 μM (Nelson et al. 2021). It is currently unclear what role(s) these helicases play in viral replication, as it could be detrimental or advantageous to the viral life cycle (Meier-Stephenson et al. 2018; Hernández-Díaz et al. 2021).

$DDX17_{135\text{-}555}$ unwinds the 3′ TR G4 using the 3′ SL

Once we established that both helicases interact with ZIKV 3′ TR, we asked if $DDX17_{135\text{-}555}$ and $DDX3X_{132\text{-}607}$ can unfold the G4 in the 3′ SL, as there is currently no evidence demonstrating that DDX3X or DDX17 unfolds G4s. The helicase assays were performed using the 3′ SL to investigate if $DDX3X_{132\text{-}607}$ and $DDX17_{135\text{-}555}$ unwind the G4 present in 3′ SL. MST helicase assay utilizes a fluorescently labeled oligo that was designed to be complementary to a portion of the target RNA that was predicted to be double-stranded, as previously described (Nelson et al. 2021). If the presence of the oligo results in a change in the migration of the fluorescently labeled molecules, we can infer that the RNA was unwound, permitting the binding to occur. The MST experiments indicated that only $DDX17_{135\text{-}555}$ caused a shift in the fluorescent migration compared to the BSA control and DDX17 mutant (Fig. 5A). An unpaired *t*-test was performed for $DDX3X_{132\text{-}607}$, $DDX17_{135\text{-}555}$, and DDX17 mutant, and the *p*-value at 95% confidence indicated a value of 0.029 for $DDX3X_{132\text{-}607}$, 0.001 for $DDX17_{135\text{-}555}$, and no statistical significance for DDX17 mutant. Collectively, these experiments suggest that the Cy5-DNA oligo binds to the unwound RNA in the presence of $DDX17_{135\text{-}555}$. The SNR ratio for $DDX17_{135\text{-}555}$ was above 5, which confirms that the assay was successful.

We also performed a spectrofluorimetric helicase assay by replacing the complimentary oligo with ThT, a G4-binding fluorescence sensor that stacks G-tetrads stabilizing K^+ ions. This system allows for the collection of the ThT fluorescence emission when it recognizes a properly folded G4 compared to unwound molecules in the presence of helicases and ATP. A fluorescence decrease was observed upon the addition of ATP into $DDX17_{135\text{-}555}$ and RNA sample, whereas for BSA, $DDX3X_{132\text{-}607}$ and DDX17 mutant showed no statistically significant change (Fig. 5B). These results suggest that $DDX17_{135\text{-}555}$ unwound the G4, specifically on the 3′ SL preventing ThT from binding/fluorescing, whereas $DDX3X_{132\text{-}607}$ and DDX17 mutant are unable to unwind the same RNA. $DDX3X_{132\text{-}607}$ and DDX17 mutant also failed to produce a significant change in the fluorescent migration of the oligo in the MST assays, which is seen in the SNR ratio, which was below 5. These combined results demonstrate a previously unreported function of $DDX17_{135\text{-}555}$: unwinding of a G4. The MST studies also demonstrate that while $DDX17_{135\text{-}555}$ can unfold the 3′ SL G4, $DDX3X_{132\text{-}607}$ cannot.

Discussion

Our work demonstrates the presence of G4 in ZIKV 3′ TR and establishes that human helicase $DDX17_{135\text{-}555}$ can unwind the G4 structure. These results unveil a previously unreported function of DDX17. Further work is required to elucidate the function(s) of the 3′ TR G4 in the ZIKV life cycle. DDX3X has been extensively studied for its ability to interact with various RNA structures, including G4 (Herdy et al. 2018). Consistent with this finding, our previous study demonstrated the capacity of $DDX3X_{132\text{-}607}$ unwinding secondary structure within the ZIKV and Japanese Encephalitis virus 5′ TRs (Nelson et al. 2021). We hypothesize that the observed inability to unwind G4 structures might be attributed to a structural feature within the substrate rather than the absence of a functional domain within the helicase. However, it is still unclear whether DDX3X can unwind G4s (H. Liu et al. 2021; Caterino and Paeschke 2022). Previous literature porposes hypotheses into the role of G4s in the 3′ TR of the viral genome, such as serving as a "capped" degradation-resistant region comparable to G overhangs in telomeres, evasion of the host intracellular immune response, assisting in viral transcription initiation, or act as another element in host protein "sponging," as this structure is contained in subflaviviral RNA (Moon et al. 2015; Lista et al. 2017; Reznichenko et al. 2019; Michalski et al. 2019; Bryan 2020). Moreover, protein sponging could also be assisted with a G4 serving as a nucleation point for RNA phase separation, potentially giving the virus more control of ion proximity and structural

Fig. 5. DDX17$_{135\text{-}555}$ unfolds the 3′ SL G4. (A) and (B) are the helicase assay experiments performed using microscale thermophoresis (A) and fluorescence spectroscopy (B). Experiments in (A) contain the complementary-labeled oligonucleotide that base pairs to the G4 sequence if unfolded by the helicase protein in the presence of ATP with the relative fluorescence represented ($n = 4$). During this binding check, it is essential to run a BSA control alongside each individual sample being tested, as BSA is the reference point for each individual run. The significance of these runs is the signal-to-noise (SNR) in the fluorescence difference. The fluorescence spectroscopy in (B) contains the G4 binding biosensor, ThT with the relative fluorescence differences measured between the presence and absence of ATP in the reaction mixture ($n = 3$). The decrease in fluorescence in (B) indicates that the G4 is unfolding in the 3′ SL; hence, ThT is unable to bind. Similar to the microscale thermophoresis (MST) analysis in A, the fluorescence in (B) need not be normalized, as a comparison of the highest fluorescence peaks within each measurement is collected. When comparing the fluorescence, it was performed in pairs, each with a BSA control for the individual proteins, rather than a comparison of the different proteins against each other. In (A), statistically significant shifts in each assay indicate that the oligo is bound to the 3′ SL. A *t*-test was performed for all assays to signify the statistical relevance of our data. The asterisks indicate the *p*-value (ns = $p > 0.05$, $^{*}p \leq 0.05$, $^{**}p \leq 0.01$, $^{***}p \leq 0.001$, $^{****}p \leq 0.0001$).

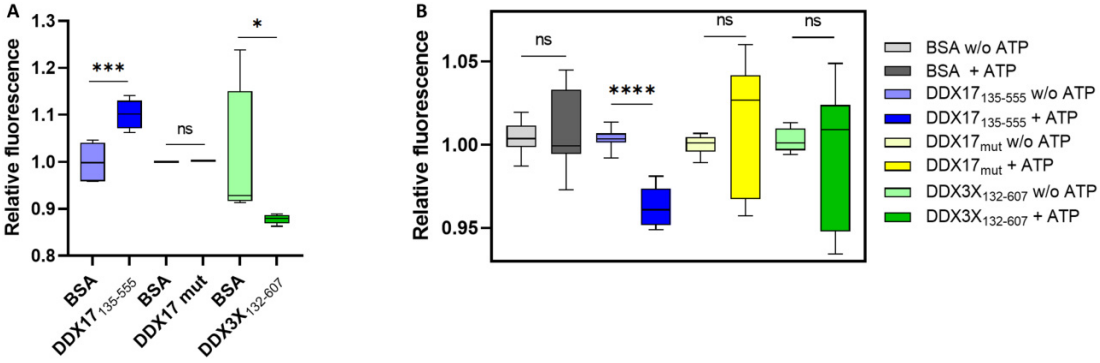

switching between a G4 and stem-loop (Bugaut et al. 2012; X. Liu et al. 2021). This would potentially provide ZIKV an extension of the number of human proteins that can be recruited to the terminal regions as well, thus providing a more streamlined replication. Furthermore, it has also been shown that the 12 regions of the 3′ TR contain N6-methyladenosines (m^{6}A) enrichment, and eight out of the 12 m^{6}A regions were on the 3′ SL G4. Previous literature showed that in the case of ZIKV, when m^{6}A was suppressed, it increased viral replication, suggesting that m^{6}A could be a mechanism the cell uses to slow viral replication (Fleming et al. 2019). Overall, further investigation into the role of G4 from ZIKV 3′ TR is required.

ZIKV remains a significant public health concern globally, and due to concerns of potential antibody-dependent enhancement caused by antibodies generated from flaviviral vaccines or infection, novel treatment avenues to stop viral replication are urgently required. To this end, our study demonstrated that ZIKV contains a G4 within the 3′ SL of the 3′ TR that is maintained across multiple ZIKV isolates and is unfolded by human DDX17$_{135\text{-}555}$. This discovery allows for further investigation to exploit this structured region by providing potential treatments using G4 binding molecules or other molecules that disrupt human DDX17–3′ SL interaction. Further studies of the function of the 3′ SL G4 during viral replication are essential, but the foundation of the identification of the G4 and two RNA-binding proteins allows for a benchmark to start exploring this region as a target to attempt to stop ZIKV replication, providing a novel treatment for ZIKV infection.

Acknowledgement

This project was funded by an NSERC Discovery Grant to TRP (RPGIN 2017–04003 and RPGIN 2022–03391). DLG's and CRN stipends were supported by NSERC Discovery Grant to TRP and Alberta Innovates, respectively. Infrastructure support was provided by the Canadian Foundation for Innovation grant to TRP (CFI 37115). MDB's and HSP's salaries were supported by a Canada Research Chair stipend and Alberta Innovates grants to TRP. TRP acknowledges the Canada Research Chair program.

Article information

History dates

Received: 14 February 2023
Accepted: 19 September 2023
Accepted manuscript online: 29 September 2023
Version of record online: 23 October 2023

Data availability

All data have been presented in this article.

Author information

Author ORCIDs

Higor S. Pereira https://orcid.org/0000-0003-4761-8361
Liam Kerr https://orcid.org/0000-0002-5459-4639
Michael T. Wolfinger https://orcid.org/0000-0003-0925-5205
Trushar R. Patel https://orcid.org/0000-0003-0627-2923

Author notes

Present address for Michael T. Wolfinger is Bioinformatics Group, Department of Computer Science, University of Freiburg, Georges-Köhler-Allee 106, 79110 Freiburg, Germany.

Dannielle L. Gemmill and Corey R. Nelson contributed equally to this work.

Trushar R. Patel served as an Editorial Board Member at the time of manuscript review and acceptance; peer review and editorial decisions regarding this manuscript were handled by another Editorial Board Member.

Author contributions

Conceptualization: TRP
Data curation: DLG, CRN, HSP, LK
Formal analysis: DLG, CRN, MDB, HSP, MTW
Funding acquisition: TRP
Investigation: MDB, TRP
Methodology: DLG, CRN, HSP, MTW
Project administration: TRP
Software: MTW
Supervision: TRP
Writing – original draft: DLG, CRN, MDB
Writing – review & editing: DLG, HSP, MTW

Competing interests

The authors declare no competing interests.

Supplementary material

Supplementary data are available with the article at https://doi.org/10.1139/bcb-2023-0036.

References

Ali, M.A.M. 2021a. The DEAD-box protein family of RNA helicases: sentinels for a myriad of cellular functions with emerging roles in tumorigenesis. Int. J. Clin. Oncol. **26**: 795–825. doi:10.1007/s10147-021-01892-1. PMID: 33656655.

Ali, M.A.M. 2021b. DEAD-box RNA helicases: the driving forces behind RNA metabolism at the crossroad of viral replication and antiviral innate immunity. Virus Res. **296**: 198352. doi:10.1016/j.virusres.2021.198352. PMID: 33640359.

Andrisani, O., Liu, Q., Kehn, P., Leitner, W.W., Moon, K., Vazquez-Maldonado, N., et al. 2022. Biological functions of DEAD/DEAH-box RNA helicases in health and disease. Nat. Immunol. **23**: 354–357. doi:10.1038/s41590-022-01149-7. PMID: 35194205.

Ariumi, Y., Kuroki, M., Abe, K., Dansako, H., Ikeda, M., Wakita, T., and Kato, N. 2007. DDX3 DEAD-box RNA helicase is required for hepatitis C virus RNA replication. J. Virol. **81**: 13922–13926. doi:10.1128/JVI.01517-07. PMID: 17855521.

Barzon, L., Pacenti, M., Franchin, E., Lavezzo, E., Trevisan, M., Sgarabotto, D., and Palù, G. 2016. Infection dynamics in a traveller with persistent shedding of Zika virus RNA in semen for six months after returning from Haiti to Italy, January 2016. Euro. Surveill. **21**:30316

Beaver, J.T., Lelutiu, N., Habib, R., and Skountzou, I. 2018. Evolution of two major Zika virus lineages: implications for pathology, immune response, and vaccine development. Front. Immunol. **9**: 1640. doi:10.3389/fimmu.2018.01640. PMID: 30072993.

Bhattacharyya, D., Mirihana Arachchilage, G., and Basu, S. 2016. Metal cations in G-quadruplex folding and stability. Front. Chem. **4**: 38. doi:10.3389/fchem.2016.00038. PMID: 27668212.

Biffi, G., Tannahill, D., Mccafferty, J., and Balasubramanian, S. 2013. Quantitative visualization of DNA G-quadruplex structures in human cells. Nat. Chem. **5**: 182–186. doi:10.1038/nchem.1548. PMID: 23422559.

Biffi, G., di Antonio, M., Tannahill, D., and Balasubramanian, S. 2014a. Visualization and selective chemical targeting of RNA G-quadruplex structures in the cytoplasm of human cells. Nat. Chem. **6**: 75–80. doi:10.1038/nchem.1805. PMID: 24345950.

Biffi, G., Tannahill, D., Miller, J., Howat, W.J., and Balasubramanian, S. 2014b. Elevated levels of G-quadruplex formation in human stomach and liver cancer tissues. PLoS One, **9**: e102711. doi:10.1371/journal.pone.0102711. PMID: 25033211.

Brai, A., Martelli, F., Riva, V., Garbelli, A., Fazi, R., Zamperini, C., et al. 2019. DDX3X Helicase inhibitors as a new strategy to fight the West Nile virus infection. J. Med. Chem. **62**: 2333–2347. doi:10.1021/acs.jmedchem.8b01403. PMID: 30721061.

Brázda, V., Hároníková, L., Liao, J.C., and Fojta, M. 2014. DNA and RNA quadruplex-binding proteins. Int. J. Mol. Sci. **15**: 17493–17517. doi:10.3390/ijms151017493. PMID: 25268620.

Bryan, T.M. 2020. G-quadruplexes at Telomeres: friend or foe? Molecules, **25**:3686. doi:10.3390/molecules25163686. PMID: 32823549.

Bugaut, A., Murat, P., and Balasubramanian, S. 2012. An RNA hairpin to G-quadruplex conformational transition. J. Am. Chem. Soc. **134**: 19953–19956. doi:10.1021/ja308665g. PMID: 23190255.

Burge, S., Parkinson, G.N., Hazel, P., Todd, A.K., and Neidle, S. 2006. Quadruplex DNA: sequence, topology and structure. Nucleic Acids Res. **34**: 5402–5415. doi:10.1093/nar/gkl655. PMID: 17012276.

Byrd, A.K., Zybailov, B.L., Maddukuri, L., Gao, J., Marecki, J.C., Jaiswal, M., et al. 2016. Evidence that G-quadruplex DNA accumulates in the cytoplasm and participates in stress granule assembly in response to oxidative stress. J. Biol. Chem. **291**: 18041–18057. doi:10.1074/jbc.M116.718478. PMID: 27369081.

Canesin, G., Di Ruscio, A., Li, M., Ummarino, S., Hedblom, A., Choudhury, R., et al. 2020. Scavenging of labile heme by Hemopexin is a key checkpoint in cancer growth and metastases. Cell Rep. **32**: 108181. doi:10.1016/j.celrep.2020.108181. PMID: 32966797.

Caterino, M., and Paeschke, K. 2022. Action and function of helicases on RNA G-quadruplexes. Methods, **204**: 110–125. doi:10.1016/j.ymeth.2021.09.003. PMID: 34509630.

Chavali, P.L., Stojic, L., Meredith, L.W., Joseph, N., Nahorski, M.S., Sanford, T.J., et al. 2017. Neurodevelopmental protein Musashi-1 interacts with the Zika genome and promotes viral replication. Science, **357**: 83–88. doi:10.1126/science.aam9243. PMID: 28572454.

Clamp, M., Cuff, J., Searle, S.M., and Barton, G.J. 2004. The Jalview Java alignment editor. Bioinformatics, **20**: 426–427. doi:10.1093/bioinformatics/btg430. PMID: 14960472.

Clark, K., Karsch-Mizrachi, I., Lipman, D.J., Ostell, J., and Sayers, E.W. 2016. GenBank. Nucleic Acids Res. **44**: D67–D72. doi:10.1093/nar/gkv1276. PMID: 26590407.

Dardenne, E., Polay Espinoza, M., Fattet, L., Germann, S., Lambert, M.P., Neil, H., et al. 2014. RNA helicases DDX5 and DDX17 dynamically orchestrate transcription, miRNA, and splicing programs in cell differentiation. Cell Rep. **7**: 1900–1913. doi:10.1016/j.celrep.2014.05.010. PMID: 24910439.

David, A.P., Pipier, A., Pascutti, F., Binolfi, A., Weiner, A.M.J., Challier, E., et al. 2019. CNBP controls transcription by unfolding DNA G-quadruplex structures. Nucleic Acids Res. **47**: 7901–7913. doi:10.1093/nar/gkz527. PMID: 31219592.

Donald, C.L., Brennan, B., Cumberworth, S.L., Rezelj, V.V., Clark, J.J., Cordeiro, M.T., et al. 2016. Full genome sequence and sfRNA interferon antagonist activity of Zika virus from Recife, Brazil. PLoS Negl. Trop. Dis. **10**: e0005048. doi:10.1371/journal.pntd.0005048. PMID: 27706161.

Dupuis, N.F., Holmstrom, E.D., and Nesbitt, D.J. 2014. Molecular-crowding effects on single-molecule RNA folding/unfolding thermodynamics and kinetics. Proceedings of the National Academy of Sciences, **111**: 8464–8469. doi:10.1073/pnas.1316039111.

Fay, M.M., Lyons, S.M., and Ivanov, P. 2017. RNA G-quadruplexes in biology: principles and molecular mechanisms. J. Mol. Biol., **429**: 2127–2147. doi:10.1016/j.jmb.2017.05.017. PMID: 28554731.

Fleming, A.M., Ding, Y., Alenko, A., and Burrows, C.J. 2016. Zika virus genomic RNA possesses conserved G-quadruplexes characteristic of the Flaviviridae Family. ACS Infect. Dis. **2**: 674–681. doi:10.1021/acsinfecdis.6b00109. PMID: 27737553.

Fleming, A.M., Nguyen, N.L.B., and Burrows, C.J. 2019. Colocalization of m (6) A and G-quadruplex-forming sequences in viral RNA (HIV, Zika, Hepatitis B, and SV40) suggests topological control of adenosine N (6)-methylation. ACS Cent. Sci. **5**: 218–228. doi:10.1021/acscentsci.8b00963. PMID: 30834310.

Fortuna, T.R., Kour, S., Anderson, E.N., Ward, C., Rajasundaram, D., Donnelly, C.J., et al. 2021. DDX17 is involved in DNA damage repair and modifies FUS toxicity in an RGG-domain dependent manner. Acta Neuropathol. **142**: 515–536. doi:10.1007/s00401-021-02333-z. PMID: 34061233.

Herdy, B., Mayer, C., Varshney, D., Marsico, G., Murat, P., Taylor, C., et al. 2018. Analysis of NRAS RNA G-quadruplex binding proteins reveals DDX3X as a novel interactor of cellular G-quadruplex containing transcripts. Nucleic Acids Res. **46**: 11592–11604. doi:10.1093/nar/gky861. PMID: 30256975.

Hernández-Díaz, T., Valiente-Echeverría, F., and Soto-Rifo, R. 2021. RNA helicase DDX3: a double-edged sword for viral replication and immune signaling. Microorganisms **9**:1206. doi:10.3390/microorganisms9061206.

Hou, Y., Gan, T., Fang, T., Zhao, Y., Luo, Q., Liu, X., et al. 2022. G-quadruplex inducer/stabilizer pyridostatin targets SUB1 to promote cytotoxicity of a transplatinum complex. Nucleic Acids Res. **50**: 3070–3082. doi:10.1093/nar/gkac151. PMID: 35258624.

Huang, L., and Zhang, C. 2021. Microscale thermophoresis (MST) to detect the interaction between purified protein and small molecule. Methods Mol. Biol. **2213**: 187–193. doi:10.1007/978-1-0716-0954-5_17. PMID: 33270204.

Javadekar, S.M., Nilavar, N.M., Paranjape, A., Das, K., and Raghavan, S.C. 2020. Characterization of G-quadruplex antibody reveals differential specificity for G4 DNA forms. DNA Res. **27**:dsaa024. doi:10.1093/dnares/dsaa024. PMID: 33084858.

Ji, N., Shi, H.-Q., Fang, X.-Y., and Wu, Z.-Y. 2020. Exploring the interaction of G-quadruplex and porphyrin derivative by single protein nanopore sensing interface. Anal. Chim. Acta **1106**: 126–132. doi:10.1016/j.aca.2020.01.053. PMID: 32145840.

Johnson, R.F., Mccarthy, S.E., Godlewski, P.J., and Harty, R.N. 2006. Ebola virus VP35-VP40 interaction is sufficient for packaging 3E-5E minigenome RNA into virus-like particles. J. Virol. **80**: 5135–5144. doi:10.1128/JVI.01857-05. PMID: 16698994.

Kikin, O., D'antonio, L., and Bagga, P.S. 2006. QGRS Mapper: a web-based server for predicting G-quadruplexes in nucleotide sequences. Nucleic Acids Res. **34**: W676–W682. doi:10.1093/nar/gkl253. PMID: 16845096.

Komůrková, D., Svobodová Kovaříková, A., and Bártová, E. 2021. G-quadruplex structures colocalize with transcription factories and nuclear speckles surrounded by acetylated and dimethylated histones H3. Int. J. Mol. Sci. **22**:1995. doi:10.3390/ijms22041995.

Kynast, R.G., Okagaki, R.J., Galatowitsch, M.W., Granath, S.R., Jacobs, M.S., Stec, A.O., et al. 2004. Dissecting the maize genome by using chromosome addition and radiation hybrid lines. Proc. Natl. Acad. Sci. USA **101**: 9921–9926. doi:10.1073/pnas.0403421101. PMID: 15197265.

Lednicky, J., Beau De Rochars, V.M., El Badry, M., Loeb, J., Telisma, T., Chavannes, S., et al. 2016. Zika virus outbreak in Haiti in 2014: molecular and clinical data. PLoS Negl. Trop. Dis. **10**: e0004687. doi:10.1371/journal.pntd.0004687. PMID: 27111294.

Li, P., Wei, Y., Mei, M., Tang, L., Sun, L., Huang, W., et al. 2018. Integrative analysis of Zika virus genome RNA structure reveals critical determinants of viral infectivity. Cell Host Microbe **24**: 875–886. doi:10.1016/j.chom.2018.10.011. PMID: 30472207.

Linder, P., Lasko, P.F., Ashburner, M., Leroy, P., Nielsen, P.J., Nishi, K., et al. 1989. Birth of the D-E-A-D box. Nature **337**: 121–122. doi:10.1038/337121a0. PMID: 2563148.

Lista, M.J., Martins, R.P., Billant, O., Contesse, M.A., Findakly, S., Pochard, P., et al. 2017. Nucleolin directly mediates Epstein-Barr virus immune evasion through binding to G-quadruplexes of EBNA1 mRNA. Nat. Commun. **8**: 16043. doi:10.1038/ncomms16043. PMID: 28685753.

Liu, H., Lu, Y.-N., Paul, T., Periz, G., Banco, M.T., Ferré-D'amaré, A.R., et al. 2021. A helicase unwinds hexanucleotide repeat RNA G-quadruplexes and facilitates repeat-associated non-AUG translation. J. Am. Chem. Soc. **143**: 7368–7379. doi:10.1021/jacs.1c00131. PMID: 33855846.

Liu, X., Xiong, Y., Zhang, C., Lai, R., Liu, H., Peng, R., et al. 2021. G-quadruplex-induced liquid-liquid phase separation in biomimetic protocells. J. Am. Chem. Soc. **143**: 11036–11043. doi:10.1021/jacs.1c03627. PMID: 34270902.

Majee, P., Pattnaik, A., Sahoo, B.R., Shankar, U., Pattnaik, A.K., Kumar, A., and Nayak, D. 2021. Inhibition of Zika virus replication by G-quadruplex-binding ligands. Mol. Ther. Nucleic Acids **23**: 691–701. doi:10.1016/j.omtn.2020.12.030. PMID: 33575115.

Mansuy, J.M., Dutertre, M., Mengelle, C., Fourcade, C., Marchou, B., Delobel, P., et al. 2016. Zika virus: high infectious viral load in semen, a new sexually transmitted pathogen? Lancet Infect. Dis. **16**: 405. doi:10.1016/S1473-3099(16)00138-9. PMID: 26949027.

Mao, S.Q., Ghanbarian, A.T., Spiegel, J., Martínez Cuesta, S., Beraldi, D., Di Antonio, M., et al. 2018. DNA G-quadruplex structures mold the DNA methylome. Nat. Struct. Mol. Biol. **25**: 951–957. doi:10.1038/s41594-018-0131-8. PMID: 30275516.

Meier-Stephenson, V., Mrozowich, T., Pham, M., and Patel, T.R. 2018. DEAD-box helicases: the yin and yang roles in viral infections. Biotechnol. Genet. Eng. Rev. **34**: 3–32. doi:10.1080/02648725.2018.1467146. PMID: 29742983.

Meinke, G., Phelan, P.J., Shin, J., Gagnon, D., Archambault, J., Bohm, A., and Bullock, P.A. 2016. Structural based analyses of the JC virus T-antigen F258L mutant provides evidence for DNA dependent conformational changes in the C-termini of polyomavirus origin binding domains. PLoS Pathog. **12**: e1005362. doi:10.1371/journal.ppat.1005362. PMID: 26735515.

Métifiot, M., Amrane, S., Litvak, S., and Andreola, M.L. 2014. G-quadruplexes in viruses: function and potential therapeutic applications. Nucleic Acids Res. **42**: 12352–12366. doi:10.1093/nar/gku999. PMID: 25332402.

Michalski, D., Ontiveros, J.G., Russo, J., Charley, P.A., Anderson, J.R., Heck, A.M., et al. 2019. Zika virus noncoding sfRNAs sequester multiple host-derived RNA-binding proteins and modulate mRNA decay and splicing during infection. J. Biol. Chem. **294**: 16282–16296. doi:10.1074/jbc.RA119.009129. PMID: 31519749.

Moon, S.L., Dodd, B.J., Brackney, D.E., Wilusz, C.J., Ebel, G.D., and Wilusz, J. 2015. Flavivirus sfRNA suppresses antiviral RNA interference in cultured cells and mosquitoes and directly interacts with the RNAi machinery. Virology **485**: 322–329. doi:10.1016/j.virol.2015.08.009. PMID: 26331679.

Morris, M.J., Wingate, K.L., Silwal, J., Leeper, T.C., and Basu, S. 2012. The porphyrin TmPyP4 unfolds the extremely stable G-quadruplex in MT3-MMP mRNA and alleviates its repressive effect to enhance translation in eukaryotic cells. Nucleic Acids Res. **40**: 4137–4145. doi:10.1093/nar/gkr1308. PMID: 22266651.

Moruno-Manchon, J.F., Koellhoffer, E.C., Gopakumar, J., Hambarde, S., Kim, N., Mccullough, L.D., and Tsvetkov, A.S. 2017. The G-quadruplex DNA stabilizing drug pyridostatin promotes DNA damage and downregulates transcription of Brca1 in neurons. Aging (Albany NY) **9**: 1957–1970. doi:10.18632/aging.101282. PMID: 28904242.

Murat, P., Zhong, J., Lekieffre, L., Cowieson, N.P., Clancy, J.L., Preiss, T., et al. 2014. G-quadruplexes regulate Epstein-Barr virus–encoded nuclear antigen 1 mRNA translation. Nat. Chem. Biol. **10**: 358–364. doi:10.1038/nchembio.1479. PMID: 24633353.

Musso, D., and Gubler, D.J. 2016. Zika virus. Clin. Microbiol. Rev. **29**: 487–524. doi:10.1128/CMR.00072-15. PMID: 27029595.

Nawrocki, E.P., and Eddy, S.R. 2013. Infernal 1.1: 100-fold faster RNA homology searches. Bioinformatics, **29**: 2933–2935. doi:10.1093/bioinformatics/btt509. PMID: 24008419.

Nelson, C., Mrozowich, T., Gemmill, D.L., Park, S.M., and Patel, T.R. 2021. Human DDX3X unwinds Japanese encephalitis and Zika viral 5′ Terminal regions. Int. J. Mol. Sci. **22**:413. doi:10.3390/ijms22010413.

Nelson, C.R., Mrozowich, T., Park, S.M., D'souza, S., Henrickson, A., Vigar, J.R.J., et al. 2020. Human DDX17 unwinds Rift Valley fever virus noncoding RNAs. Int. J. Mol. Sci. **22**:54. doi:10.3390/ijms22010054.

Patel, P.K., Bhavesh, N.S., and Hosur, R.V. 2000. NMR observation of a novel C-tetrad in the structure of the SV40 repeat sequence GGGCGG. Biochem. Biophys. Res. Commun. **270**: 967–971. doi:10.1006/bbrc.2000.2479. PMID: 10772934.

Prevention, C.O.D.C.A. 2022. *Zika travel information* [Online]. https://wwwnc.cdc.gov/travel/page/zika-information

Reznichenko, O., Quillévéré, A., Martins, R.P., Loaëc, N., Kang, H., Lista, M.J., et al. 2019. Novel cationic bis (acylhydrazones) as modulators of Epstein-Barr virus immune evasion acting through disruption of interaction between nucleolin and G-quadruplexes of EBNA1 mRNA. Eur. J. Med. Chem. **178**: 13–29. doi:10.1016/j.ejmech.2019.05.042. PMID: 31173968.

Rodriguez, R., Miller, K.M., Forment, J.V., Bradshaw, C.R., Nikan, M., Britton, S., et al. 2012. Small-molecule-induced DNA damage identifies alternative DNA structures in human genes. Nat. Chem. Biol. **8**: 301–310. doi:10.1038/nchembio.780. PMID: 22306580.

Ruggiero, E., and Richter, S.N. 2020. Viral G-quadruplexes: new frontiers in virus pathogenesis and antiviral therapy. Annu. Rep. Med. Chem. **54**: 101–131. PMID: 32427223.

Sanford, T.J., Mears, H.V., Fajardo, T., Locker, N., and Sweeney, T.R. 2019. Circularization of flavivirus genomic RNA inhibits de novo translation initiation. Nucleic Acids Res. **47**: 9789–9802. doi:10.1093/nar/gkz686. PMID: 31392996.

Schneider, A.D.B., and Wolfinger, M.T. 2019. Musashi binding elements in Zika and related flavivirus 3′UTRs: a comparative study in silico. Sci. Rep. **9**: 6911. doi:10.1038/s41598-019-43390-5. PMID: 31061405.

Sirohi, D., and Kuhn, R.J. 2017. Zika virus structure, maturation, and receptors. J. Infect. Dis. **216**: S935–s944. doi:10.1093/infdis/jix515. PMID: 29267925.

Tang, B.L. 2016. Zika virus as a causative agent for primary microencephaly: the evidence so far. Arch. Microbiol. **198**: 595–601. doi:10.1007/s00203-016-1268-7. PMID: 27412681.

Tanner, N.K., Cordin, O., Banroques, J., Doère, M., and Linder, P. 2003. The Q motif: a newly identified motif in DEAD box helicases may regulate ATP binding and hydrolysis. Mol. Cell **11**: 127–138. doi:10.1016/S1097-2765(03)00006-6. PMID: 12535527.

USA Food and Drug Administration. 2022. *Zika Virus Response Updates from FDA* [Online]. https://www.fda.gov/emergency-preparedness-and-response/mcm-issues/zika-virus-response-updates-fda

Varshney, D., Cuesta, S.M., Herdy, B., Abdullah, U.B., Tannahill, D., and Balasubramanian, S. 2021. RNA G-quadruplex structures control ribosomal protein production. Sci. Rep. **11**: 22735. doi:10.1038/s41598-021-01847-6. PMID: 34815422.

Wang, Y., and Patel, D.J. 1993. Solution structure of a parallel-stranded G-quadruplex DNA. J. Mol. Biol. **234**: 1171–1183. doi:10.1006/jmbi.1993.1668. PMID: 8263919.

Will, S., Reiche, K., Hofacker, I.L., Stadler, P.F., and Backofen, R. 2007. Inferring noncoding RNA families and classes by means of genome-scale structure-based clustering. PLoS Comput. Biol. **3**: e65. doi:10.1371/journal.pcbi.0030065. PMID: 17432929.

Wolfinger, M.T. 2021. Functional RNA structures in the 3'UTR of Mosquito-Borne flaviviruses. Virus Bioinformatics,pp. 65–100.

Xu, S., Li, Q., Xiang, J., Yang, Q., Sun, H., Guan, A., et al. 2016. Thioflavin T as an efficient fluorescence sensor for selective recognition of RNA G-quadruplexes. Sci. Rep. **6**: 24793. doi:10.1038/srep24793. PMID: 27098781.

Xu, Y.Z., Jenjaroenpun, P., Wongsurawat, T., Byrum, S.D., Shponka, V., Tannahill, D., et al. 2020. Activation-induced cytidine deaminase localizes to G-quadruplex motifs at mutation hotspots in lymphoma. NAR Cancer, **2**: zcaa029. doi:10.1093/narcan/zcaa029. PMID: 33094287.

Yoo, B.C., Kragler, F., Varkonyi-Gasic, E., Haywood, V., Archer-Evans, S., Lee, Y.M., et al. 2004. A systemic small RNA signaling system in plants. Plant Cell **16**: 1979–2000. doi:10.1105/tpc.104.023614. PMID: 15258266.

Zamiri, B., Reddy, K., Macgregor, R.B., Jr., and Pearson, C.E. 2014. TMPyP4 Porphyrin distorts RNA G-quadruplex structures of the disease-associated r (GGGGCC)n repeat of the C9orf72 gene and blocks interaction of RNA-binding proteins. J. Biol. Chem. **289**: 4653–4659. PMID: 24371143.

Zhang, S., Wu, Y., and Zhang, W. 2014. G-quadruplex structures and their interaction diversity with ligands. ChemMedChem **9**: 899–911. doi:10.1002/cmdc.201300566. PMID: 24729465.

Zhang, X., Spiegel, J., Martínez Cuesta, S., Adhikari, S., and Balasubramanian, S. 2021. Chemical profiling of DNA G-quadruplex-interacting proteins in live cells. Nat. Chem. **13**: 626–633. doi:10.1038/s41557-021-00736-9. PMID: 34183817.

Zou, M., Li, J.Y., Zhang, M.J., Li, J.H., Huang, J.T., You, P.D., et al. 2021. G-quadruplex binder pyridostatin as an effective multi-target ZIKV inhibitor. Int. J. Biol. Macromol. **190**: 178–188. doi:10.1016/j.ijbiomac.2021.08.121. PMID: 34461156.